

מכון ויצמן למדע

WEIZMANN INSTITUTE OF SCIENCE



Elucidating the atomistic origin of anharmonicity in tetragonal $\text{CH}_3\text{NH}_3\text{PbI}_3$ with Raman scattering

Document Version:

Accepted author manuscript (peer-reviewed)

Citation for published version:

Sharma, R, Dai, Z, Gao, L, Brenner, TM, Yadgarov, L, Zhang, J, Rakita, Y, Korobko, R, Rappe, AM & Yaffe, O 2020, 'Elucidating the atomistic origin of anharmonicity in tetragonal $\text{CH}_3\text{NH}_3\text{PbI}_3$ with Raman scattering', *Physical Review Materials*, vol. 4, no. 9, 092401.
<https://doi.org/10.1103/PhysRevMaterials.4.092401>

Total number of authors:

10

Digital Object Identifier (DOI):

[10.1103/PhysRevMaterials.4.092401](https://doi.org/10.1103/PhysRevMaterials.4.092401)

Published In:

Physical Review Materials

License:

Other

General rights

@ 2020 This manuscript version is made available under the above license via The Weizmann Institute of Science Open Access Collection is retained by the author(s) and / or other copyright owners and it is a condition of accessing these publications that users recognize and abide by the legal requirements associated with these rights.

How does open access to this work benefit you?

Let us know @ library@weizmann.ac.il

Take down policy

The Weizmann Institute of Science has made every reasonable effort to ensure that Weizmann Institute of Science content complies with copyright restrictions. If you believe that the public display of this file breaches copyright please contact library@weizmann.ac.il providing details, and we will remove access to the work immediately and investigate your claim.

Elucidating the atomistic origin of anharmonicity in tetragonal $\text{CH}_3\text{NH}_3\text{PbI}_3$ with Raman scatteringRituraj Sharma^{1,*}, Zhenbang Dai^{2,*}, Lingyuan Gao², Thomas M. Brenner¹, Lena Yadgarov¹, Jiahao Zhang², Yevgeny Rakita¹, Roman Korobko¹, Andrew M. Rappe^{2,†} and Omer Yaffe^{1,‡}¹Department of Materials and Interfaces, Weizmann Institute of Science, Rehovot 76100, Israel²Department of Chemistry, University of Pennsylvania, Philadelphia, Pennsylvania 19104-6323, USA

(Received 17 April 2020; revised 16 July 2020; accepted 31 July 2020; published 1 September 2020)

Halide perovskite (HP) semiconductors exhibit unique strong coupling between the electronic and structural dynamics. We use Raman polarization-orientation (PO) measurements and *ab initio* molecular dynamics (AIMD) to investigate the origin and temperature evolution of the strong structural anharmonicity throughout the tetragonal phase of $\text{CH}_3\text{NH}_3\text{PbI}_3$. Raman PO measurements reveal a soft modelike spectral feature. This mode shows an unusual continuous increase in damping with temperature which is indicative of an anharmonic potential surface. The analysis of AIMD trajectories identifies two major sources of anharmonicity: the orientational unlocking of the $[\text{CH}_3\text{NH}_3]^+$ ions and large-amplitude octahedral tilting that continuously increases with temperature. Our work suggests that the standard phonon picture cannot describe the structural dynamics of tetragonal $\text{CH}_3\text{NH}_3\text{PbI}_3$.

DOI: 10.1103/PhysRevMaterials.4.092401

Methylammonium lead iodide (MAPI) has emerged as an outstanding absorber material for photovoltaics [1–3]. Recent evidence indicates that the beneficial optical and electronic properties of halide perovskites (HPs) are intimately associated with their unusual structural dynamics and mechanical softness [4]. The cubic phase of HPs was shown to exhibit strongly anharmonic thermal fluctuations with light scattering properties that resemble those of liquids [5–8]. Yet, little is known about the atomistic origin and nature of structural dynamics of the room-temperature tetragonal phase of MAPI.

MAPI crystallizes into an ABX_3 -type perovskite structure, with PbI_6 in a corner-sharing octahedral network, and MA molecules inside the cuboctahedral cavities. It shows two structural phase transitions: $Pnma$, orthorhombic (o) to $I4/mcm$ or $I4cm$, tetragonal (t) at ≈ 162 K, and tetragonal to $Pm\bar{3}m$, cubic (c) at ≈ 327 K [5,9]. Similar to other perovskite crystals, the calculated harmonic phonon dispersion relation of the cubic phase of MAPI shows imaginary frequencies [10,11], which indicates that the cubic structure has double wells in its potential-energy surface and thus is entropically stabilized (i.e., strongly anharmonic) [10,12]. On the other hand, the orthorhombic phase does not have any imaginary frequency modes, consistent with current expectations that MAPI exhibits mostly harmonic behavior in the orthorhombic phase [13].

Interestingly, the phonon dispersion relation of the t phase of MAPI does not exhibit imaginary frequencies [11,14], implying the stability of the tetragonal structure. Nevertheless, many seemingly contradictory characteristics that prevail at room temperature in the t phase, such as low mobility but high

carrier lifetime, and small Urbach energy but high density of structural defects [4,15,16], cannot be explained in a harmonic picture but point toward strong structural anharmonicity also in the t phase. The conflict between the harmonic phonon picture and the experimentally observed anomalies has inspired several works which take the anharmonicity of the t phase into consideration. These works show how anharmonicity influences the electronic properties [17,18], and attempts have been made to understand the origin and mechanism of anharmonicity [19,20]. However, most of the focus has been on the cubic phase, and a detailed atomistic description in the frequency and time domains and its evolution with temperature is still missing, making the nature and mechanisms of the anharmonicity in t -phase MAPI a largely unanswered question.

In this Rapid Communication, we investigate the complex structural dynamics of the t phase of MAPI. Using temperature-dependent polarization-orientation (PO) Raman measurements, we discover spectral features and trends that indicate that the t phase of MAPI is strongly anharmonic. A definitive assignment of the Raman spectral features to real-space atomic motions (beyond normal-mode analysis) is obtained using *ab initio* molecular dynamics (AIMD). We employed this real-space analysis to elucidate the microscopic mechanisms governing the strongly anharmonic structural dynamics in t -MAPI.

We perform low-frequency Raman measurements on single crystals oriented along the [110] direction relative to the Bravais lattice unit cell. High-quality MAPI single crystals were grown at room temperature using the antisolvent method, as discussed elsewhere [21]. To identify the crystallographic orientation of the crystal, specular x-ray diffraction (XRD) was used (see Fig. S1 in Supplemental Material (SM) [22]). The measurement was carried out using the $\text{Cu K}\alpha$ line source in the Bragg-Brentano reflection geometry on

*These authors contributed equally to this work.

†rappe@sas.upenn.edu

‡omer.yaffe@weizmann.ac.il

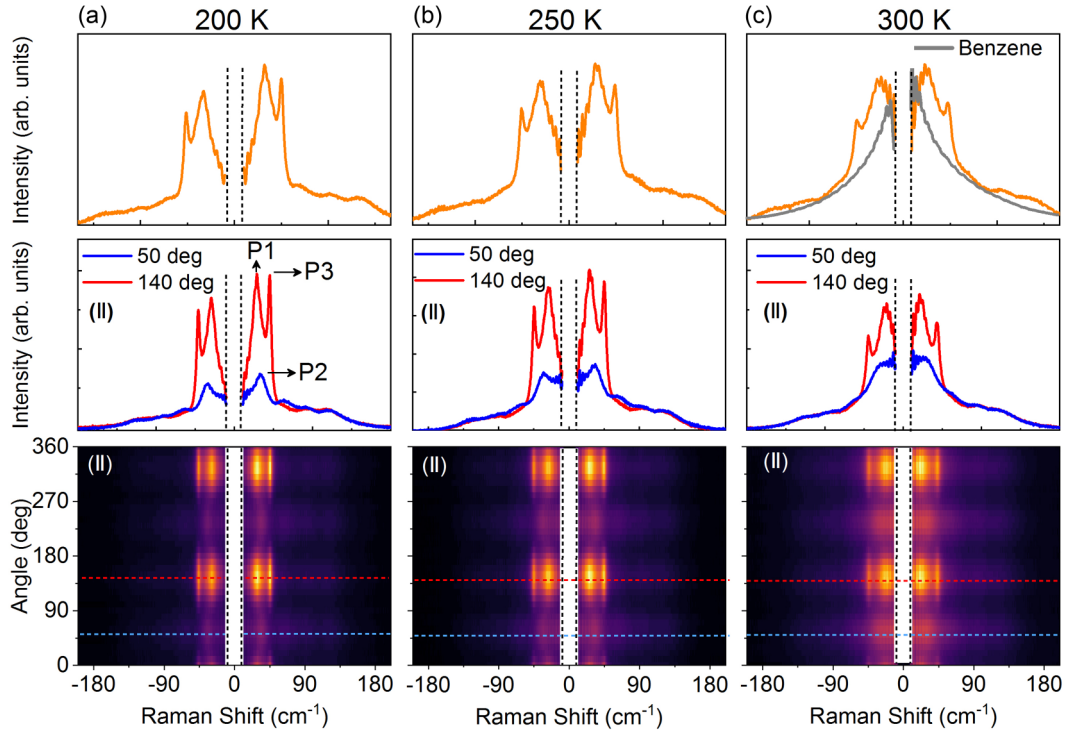


FIG. 1. Temperature evolution of PO-dependent Raman spectra of MAPI measured at (a) 200 K, (b) 250 K, and (c) 300 K. The upper panel shows the unpolarized spectra (summed over all polarization angles). The spectrum of MAPI at 300 K is compared with that of benzene in (c). Contour plots for PO dependence of the Raman spectra in the parallel configuration are shown in the bottom panel. Cross sections of the contours corresponding to the angular positions shown by dotted blue and red lines are shown in the middle panel (blue and red curves). The 0° polarization angle is arbitrarily defined and is identical for all measurements.

a Rigaku TTRAX III (18 kW) θ - θ vertical diffractometer equipped with cross beam optics (CBO). Different surfaces were measured, and the diffractograms were matched with previous results [21]. After determining the [110] surface, for which diffraction peaks corresponding to (110), (220), (330), and (440), etc., planes are obtained (as shown in Fig. S1 [22]), the sample was fixed on a Cu substrate with its [110] side facing up. The sample in the same condition was taken for Raman measurement, such that Raman experiments were performed on the [110] face.

Subband gap excitation at 1064 nm (1.16 eV) is used to overcome the damage related to the light absorption and poor thermal conductivity of MAPI that occurs with shorter-wavelength excitation. Figure 1 (top panel) shows the unpolarized Raman spectra at three different temperatures throughout the t phase, displaying both anti-Stokes and Stokes scattering. The low-temperature (200 K) spectrum shows two distinct peaks at ≈ 28 and 45 cm^{-1} . As the temperature increases, the spectrum broadens and redshifts. At 300 K, a broad spectrum with a peak near 45 cm^{-1} is observed. Interestingly, the room-temperature spectrum of MAPI resembles the Raman spectrum of a fluid. In the upper panel of Fig. 1(c), we have compared the room-temperature spectra of MAPI with benzene. The extraordinary similarity between these two spectra indicates that despite the crystalline order of the tetragonal structure, MAPI exhibits liquidlike, relaxational motions [23,24].

Next, we use PO Raman spectroscopy (Fig. 1, lower panels) to investigate the origin of structural anharmonicity in t

phase MAPI. The details of the experiment are discussed in the SM [22]. Briefly, the crystal oriented along the [110] direction is excited by plane-polarized laser light with polarization e_i . The scattered light is then filtered by another polarizer (analyzer) oriented parallel or perpendicular to the incident light. This PO measurement is repeated after each incremental rotation of the polarization of the incident light. To exclude the possibility of scattering by surface defects and domain boundaries, we performed polarized Raman measurement at 10 K [13] at different spatial positions. The uniformity and excellent agreement of the experimental and theoretical PO dependence of the Raman-active modes validates the high quality of the single crystal. We ensured that the spot size of the laser is comparable with the domain size of MAPI and that the measurements at all temperatures are carried out at the exact same point on the crystal.

The contour plots in the lower panels of Fig. 1 show the angular dependence of polarized Raman spectra for measurements performed at 200, 250, and 300 K covering the stability range of the tetragonal phase, in the parallel configuration. It is worth mentioning that the data in Fig. 1 are presented in their raw form without any normalization or baseline correction, and the results are completely reversible with temperature. These plots show a periodic modulation of the intensities of all the Raman peaks with polarization angle. The data for the cross configuration are given in the SM [22], Fig. S2. The strong and periodic oscillations in intensity are indicative of the long-range order of the crystal. In standard quasi-harmonic crystals (e.g., silicon, GaAs), the combination of parallel and

perpendicular data sets enables the extraction of the symmetry of each observed mode [25,26]. We have recently demonstrated this for the *o* phase of MAPI [13]. However, since the Raman features of the *t* phase are extremely broad and cannot be assigned to specific normal modes, the interpretation of the PO data is not as straightforward.

The low-frequency ($<50\text{ cm}^{-1}$) spectra show modulation with a 180° period in the PO dependence, resulting in two distinct line shapes at 50° and 140° PO angles, denoted by blue and red dotted lines, respectively, in Fig. 1 (bottom panel). The spectra were deconvoluted using a multi-Lorentz oscillator model (details of the fit procedure are given in the SM [22]). We identify six distinct spectral features (labeled as P1–P6). The corresponding widths and positions extracted from the fits are given in Table S1 and Figs. S3 and S4 in the SM [22]. In Fig. 1 (middle panel), we observe that all the spectral features of the 140° line shape appear in the unpolarized spectrum also (top panel). However, the $\approx 30\text{ cm}^{-1}$ feature (P2, blue curve) is undetectable in the unpolarized spectrum (top panel of Fig. 1). In that sense, it is a hidden feature.

Notably, both the relative intensity and width of P2 rapidly increase with increasing temperature (middle panel of Fig. 1). When P2 is completely overdamped (at $\approx 340\text{ K}$) a *t-c* phase transition occurs. In cubic phase, the 50° and 140° line shapes become indistinguishable and identical to the unpolarized line shape (see Fig. S5 in SM [22]). Therefore, P2 resembles a soft mode that leads to the *t-c* phase transition [27].

According to our fitted linewidth (see SM [22], Table S1), the lifetime of the Lorentz oscillator P2 becomes extremely short ($\approx 154\text{ fs}$) at room temperature, at least two orders of magnitude less than the lifetime of the standard optical phonon of crystalline silicon [28]. Using the average phonon group velocities reported elsewhere [29,30], we found that our calculated phonon mean free path is $\approx 2.2\text{ \AA}$, which is shorter than the *t*-MAPI lattice constant ($a = 8.8\text{ \AA}$, $c = 12.7\text{ \AA}$) [9]. This suggests that the standard phonon picture cannot describe the structural dynamics of the crystal. The breakdown of the phonon picture also implies that the Fröhlich interaction mechanism, which is considered to be the dominant mechanism for electron scattering in MAPI [31], is oversimplified.

To gain a microscopic understanding of the complex structural dynamics of the *t* phase of MAPI, we performed AIMD simulations. First, we use the AIMD trajectories to reproduce the experimental Raman spectra for all three phases of MAPI (Fig. S6 in SM [22]) employing the approach as in Ref. [32]. Next, we assign atomic motions to the spectral features observed in Fig. 1. We defined specific real-space ionic motions as shown in Figs. S7–S9 in the SM [22]. AIMD trajectories filtered for a narrow frequency window (0.5 cm^{-1}) were then projected onto these predefined modes in order to construct a spectrally resolved decomposition of the ionic motions. We assigned the spectral feature P2 to a symmetric distortion in the pseudocubic *xz* and *yz* plane, while the P3 feature is the analogous symmetric distortion in the *xy* plane, as shown in Fig. S10 of the SM [22]. Both P2 and P3 reflect the same distortion pattern but in different planes. Evidently, the strong damping with temperature of P2 (middle panel of Fig. 1) is indicative of strong anharmonicity in the symmetric distortion of pseudocubic *xz* and *yz* planes.

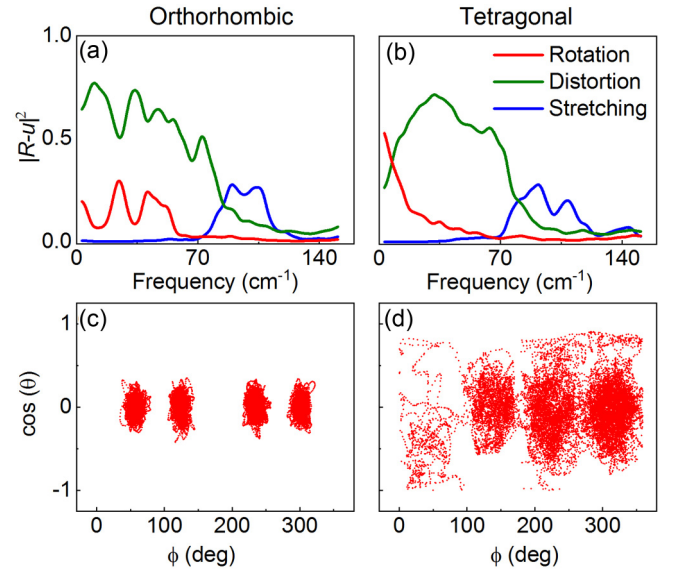


FIG. 2. The projections of frequency-filtered AIMD for the (a) orthorhombic and (b) tetragonal phases. The nearly harmonic low-frequency peaks in (a) the *o* phase representing rotations of the octahedra (red curve) are replaced (b) by a broad central feature in the *t* phase. Statistics of MA molecular orientations in the (c) *o* and (d) *t* phases. ϕ is the azimuthal angle and θ is the polar angle. The molecule is allowed to visit more orientations when it goes from the *o* to the *t* phase, indicating the onset of the molecular disorder and strong anharmonic mode couplings.

We now elucidate the structural anharmonicity that is related to the *o-t* phase transition in MAPI. To do so, we examine the spectrally resolved decomposition of the ionic motions. The weight of each mode as a function of frequency is displayed for the *o* and *t* phases in Fig. 2. The data clearly show that only octahedral distortions and rotations are dominant in the frequency region below 50 cm^{-1} . For the *o* phase shown in Fig. 2(a), two distinct peaks corresponding to PbI_6 rotational vibrations are found, and an ultralow-frequency, octahedral rotational motion (5 cm^{-1}) is also present. This is in line with our previous observations that the *o* phase is quasi-harmonic and has well-defined normal modes [13]. After the phase transition to the *t* phase Fig. 2(b), PbI_6 rotations (red) change dramatically. The well-resolved features of the *o* phase are replaced by a dominant broad feature that is centered around 0 cm^{-1} (a “central peak”) in the *t* phase. This indicates that the quasi-harmonic PbI_6 vibrations of the *o* phase have evolved to relaxational rotations in the *t* phase [33,34].

The abrupt change in Raman spectra at the *o-t* phase transition can be understood on the basis of the interactions between the lattice and the MA molecules. As described in previous works [35–37], there exists a hydrogen bonding (H bond) interaction between MA^+ cations and the negatively charged $[\text{PbI}_3]^-$ cages. At low temperatures, each PbI_6 cage does not have enough thermal kinetic energy to overcome its H-bonding interactions, and thus PbI_6 rotation is a nearly harmonic vibration (libration) [Fig. 2(c)]. Similarly, the movement of the MA molecule, either translation or rotation, is also restrained by the H bonds. At higher temperatures, increased PbI_6 rotational energy allows the octahedra to dynamically

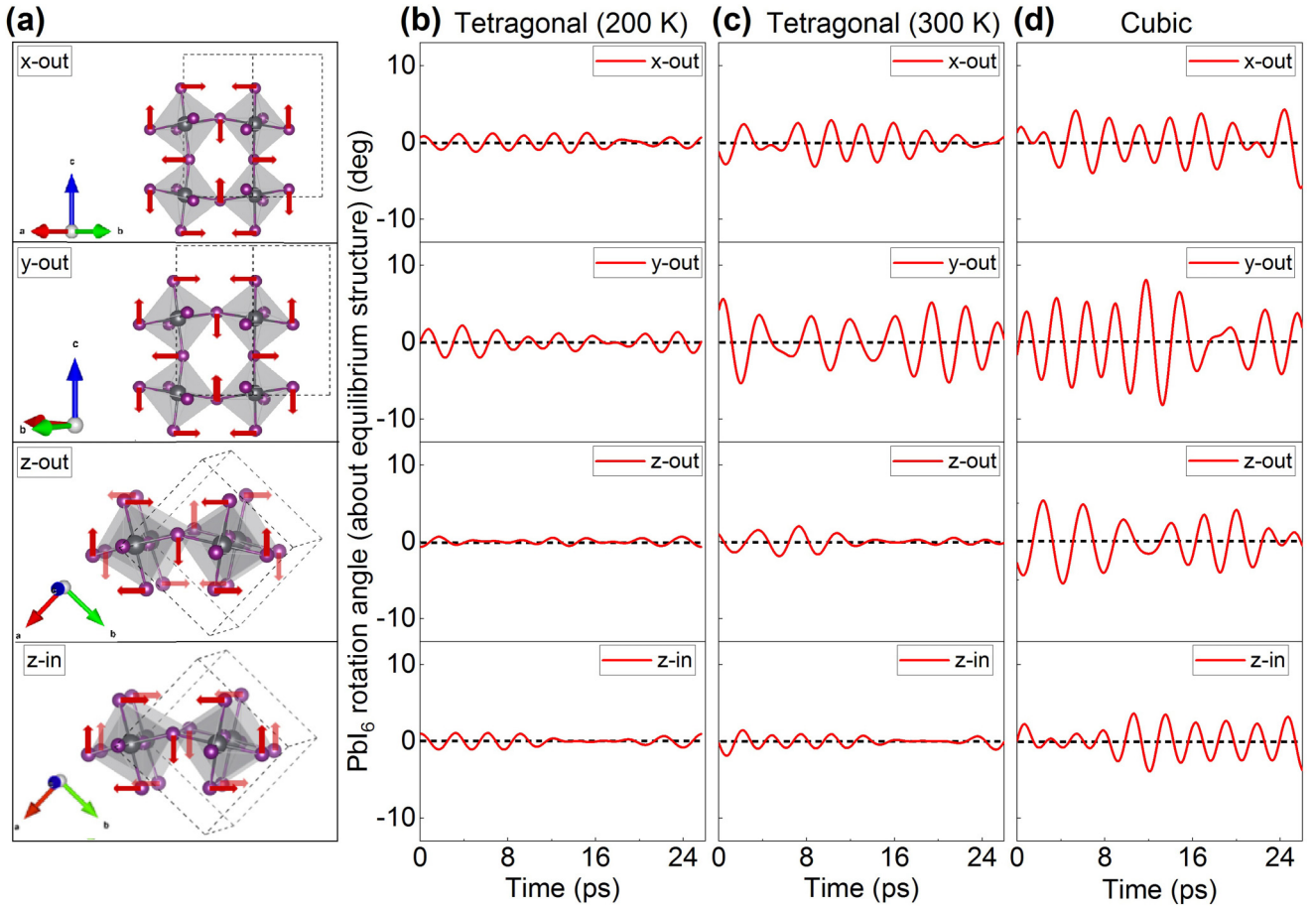


FIG. 3. Contrasting the PbI₆ rotational motions in the *t* and *c* phases. (a) Illustrations of real-space PbI₆ rotational motions. (b)–(d) Time evolution of PbI₆ rotation amplitudes in the *t* phase at (b) 200 K, (c) 300 K, and (d) the *c* phase. The legend reports the rotation axis and the relative rotation direction. For example, *x*-out represents the out-of-phase rotation along the *x* axis, and *z*-in represents the in-phase rotation along the *z* axis. These amplitudes are obtained from MD trajectories frequency-filtered to 1 cm⁻¹. The black dashed lines at 0° represent the equilibrium tilting angle of the octahedra around each axis, which has been offset to the 0° for a clearer comparison. The equilibrium angle can be found in Table S2.

break the H bonding, freeing the movement of the MA molecules. Figure 2(d) shows that the MA molecules are allowed to visit more orientations in the *t* phase. The weight of the MA translational motion below 50 cm⁻¹ also increases in the *t* phase compared to the *o* phase (Fig. S9 in SM [22]). Thus the *o*-*t* phase transition marks the onset of orientational disorder of the MA⁺ ion. In Fig. S11 in the SM [22], we present a cartoon of the octahedral cage for each phase to illustrate this special unlocking phenomenon.

Having demonstrated the advent of anharmonicity in the *t* phase, we move on to explain its evolution with increasing temperature. We decompose the low-frequency relaxational motion (≈ 1 cm⁻¹) into four different PbI₆ rotations [Fig. 3(a) and Fig. S13 in SM [22]]. The rotational motions are separated according to the rotation axis and relative direction. For example, *z*-out means the out-of-phase PbI₆ rotation along the *z* axis. Figures 3(b)–3(d) show the amplitude of the dynamic rotation for different phases. Table S2 in SM [22] tabulates the equilibrium octahedral tilting angles. Large-amplitude rotations are indicative of strongly anharmonic, relaxational motions while a small amplitude is indicative of quasi-harmonic, vibrational motion. For the *t* phase [Figs. 3(b) and

3(c)] the amplitude of the dynamic rotation around the *z* axis is small. In contrast, the rotation amplitudes about the *x* and *y* axes are quite significant, revealing strong dynamic processes occurring along these two directions. The amplitudes grow even larger as temperature increases from 200 to 300 K. This indicates that the relaxational rotation happens only around the two short axes of the tetragonal cell. Since in the *t* phase the amplitude of rotation around the *z* axis is small, the distortion in the *xy* plane is not altered and thus the corresponding peak P3 remains sharp and distinct throughout this range of temperature. In the *c* phase [Fig. 3(d)], however, PbI₆ rotations along all three axes are activated, and the equilibrium octahedral tilting angles for all three axes are close to zero (*a*⁰*a*⁰*a*⁰). Interestingly, there is a temporal phase shift between the three out-of-phase rotations (see SM [22], Fig. S14), meaning that at one time, significant rotation occurs only about one axis while for the other two axes, the rotational amplitudes are quite small. This leads to instantaneous *t*-phase structures formed along different directions. Therefore, apart from the abrupt structural rearrangements at the *o*-*t* phase transition, the PbI₆ relaxational rotation is another important source of anharmonicity that increases continuously with temperature,

and these rotations also contribute to the central peak in the Raman spectra because of the accompanied local polarization fluctuation associated with the Pb lone pair [38,39], in addition to the previously revealed off-center motion of A cations [7]. In fact, the high weight of PbI_6 rotation at low-frequency range in the mode projection [Fig. 2(b)] indicates that it is the major contribution to the central peak, and other inorganic halide perovskites could exhibit similar characteristics[7]. Our analysis clearly reflects the highly anharmonic behavior of the t phase. This contradicts the 0 K phonon dispersion computations which do not display negative frequencies [40,41].

In conclusion, we demonstrate strongly anharmonic structural dynamics and the presence of soft modelike behavior in tetragonal MAPbI₃. We have shown how the atomic motions and phase sequence are dominated by temperature-activated relaxational motion of the PbI_6 octahedra and MA molecules. The abrupt unlocking of the H bonds at the o - t phase transition marks the onset of anharmonicity. This enables the rotation of MA molecules and tilting in PbI_6 cages leading to large-amplitude anharmonic motions. The anharmonicity evolves with temperature due to the continuous damping of the PbI_6 rotational modes throughout the t phase. It ex-

plains the liquidlike relaxational behavior observed in Raman spectra and reflects the breakdown of the phonon picture in HPs.

The authors would like to thank Dr. Tsachi Livneh (NRC) for fruitful discussions, Dr. Ishay Feldman (WIS) for performing x-ray diffraction measurements, and Dr. Lior Segev (WIS) for developing the Raman software. R.S. acknowledges FGS-WIS for financial support. O.Y. acknowledges funding from ISF (1861/17), BSF (Grant No. 2016650), ERC (850041-ANHARMONIC), Benozio Endowment Fund, Ilse Katz Institute, Henry Chanoch Kreuter Institute, Sorel New Scientists Start up Fund, Carolito Stiftung, Abraham and Sonia Rochlin Foundation, E. A. Drake and R. Drake, and the Perlman Family. Z.D. and L.G. acknowledge support from the U.S. National Science Foundation, under Grant No. DMR-1719353. J.Z. acknowledges support from a VIEST Fellowship at the University of Pennsylvania. A.M.R. acknowledges support from the Department of Energy, Office of Science, Office of Basic Energy Sciences, under Grant No. DE-FG02-07ER46431. The authors acknowledge computational support from the National Energy Research Scientific Computing Center of the U.S. Department of Energy.

- [1] T. M. Brenner, D. A. Egger, L. Kronik, G. Hodes, and D. Cahen, Hybrid organic–inorganic perovskites: Low-cost semiconductors with intriguing charge-transport properties, *Nat. Rev. Mater.* **1**, 15007 (2016).
- [2] M. Grätzel, The rise of highly efficient and stable perovskite solar cells, *Acc. Chem. Res.* **50**, 487 (2017).
- [3] N. J. Jeon, J. H. Noh, Y. C. Kim, W. S. Yang, S. Ryu, and S. Il Seok, Solvent engineering for high-performance inorganic-organic hybrid perovskite solar cells, *Nat. Mater.* **13**, 897 (2014).
- [4] D. A. Egger, A. Bera, D. Cahen, G. Hodes, T. Kirchartz, L. Kronik, R. Lovrincic, A. M. Rappe, D. R. Reichman, and O. Yaffe, What remains unexplained about the properties of halide perovskites? *Adv. Mater.* **30**, 1800691 (2018).
- [5] A. Poglitsch and D. Weber, Dynamic disorder in methylammoniumtrihalogenoplumbates (II) observed by millimeter-wave spectroscopy, *J. Chem. Phys.* **87**, 6373 (1987).
- [6] M. Mayers, L. Z. Tan, D. A. Egger, A. M. Rappe, and D. R. Reichman, How lattice and charge fluctuations control carrier dynamics in halide perovskites, *Nano Lett.* **18**, 8041 (2018).
- [7] O. Yaffe, Y. Guo, L. Z. Tan, D. A. Egger, T. Hull, C. C. Stoumpos, F. Zheng, T. F. Heinz, L. Kronik, M. G. Kanatzidis, J. S. Owen, A. M. Rappe, M. A. Pimenta, and L. E. Brus, Local Polar Fluctuations in Lead Halide Perovskite Crystals, *Phys. Rev. Lett.* **118**, 136001 (2017).
- [8] L. D. Whalley, J. M. Frost, Y.-K. Jung, and A. Walsh, Perspective: Theory and simulation of hybrid halide perovskites, *J. Chem. Phys.* **146**, 220901 (2017).
- [9] P. S. Whitfield, N. Herron, W. E. Guise, K. Page, Y. Q. Cheng, I. Milas, and M. K. Crawford, Structures, phase transitions and tricritical behavior of the hybrid perovskite methyl ammonium lead iodide, *Sci. Rep.* **6**, 35685 (2016).
- [10] A. N. Beecher, O. E. Semonin, J. M. Skelton, J. M. Frost, M. W. Terban, H. Zhai, A. Alatas, J. S. Owen, A. Walsh, and S. J. L. Billinge, Direct observation of dynamic symmetry breaking above room temperature in methylammonium lead iodide perovskite, *ACS Energy Lett.* **1**, 880 (2016).
- [11] F. Brivio, J. M. Frost, J. M. Skelton, A. J. Jackson, O. J. Weber, M. T. Weller, A. R. Goñi, A. M. A. Leguy, P. R. F. Barnes, and A. Walsh, Lattice dynamics and vibrational spectra of the orthorhombic, tetragonal, and cubic phases of methylammonium lead iodide, *Phys. Rev. B* **92**, 144308 (2015).
- [12] T. Zhu and E. Ertekin, Mixed phononic and non-phononic transport in hybrid lead halide perovskites: Glass-crystal duality, dynamical disorder, and anharmonicity, *Energy Environ. Sci.* **12**, 216 (2019).
- [13] R. Sharma, M. Menahem, Z. Dai, L. Gao, T. M. Brenner, L. Yadgarov, J. Zhang, Y. Rakita, R. Korobko, I. Pinkas, A. M. Rappe, and O. Yaffe, Lattice mode symmetry analysis of the orthorhombic phase of methylammonium lead iodide using polarized Raman, *Phys. Rev. Materials* **4**, 051601(R) (2020).
- [14] M. Wang and S. Lin, Anisotropic and ultralow phonon thermal transport in organic–inorganic hybrid perovskites: Atomistic insights into solar cell thermal management and thermoelectric energy conversion efficiency, *Adv. Funct. Mater.* **26**, 5297 (2016).
- [15] S. De Wolf, J. Holovsky, S.-J. Moon, P. Löper, B. Niesen, M. Ledinsky, F.-J. Haug, J.-H. Yum, and C. Ballif, Organometallic halide perovskites: Sharp optical absorption edge and its relation to photovoltaic performance, *J. Phys. Chem. Lett.* **5**, 1035 (2014).
- [16] A. Walsh, P. Azarhoosh, S. McKechnie, M. van Schilfgaarde, and J. M. Frost, Research update: Relativistic origin of slow electron-hole recombination in hybrid halide perovskite solar cells, *APL Mater.* **4**, 091501 (2016).
- [17] K. T. Munson, E. R. Kennehan, G. S. Doucette, and J. B. Asbury, Dynamic disorder dominates delocalization, transport, and recombination in halide perovskites, *Chem* **4**, 2826 (2018).

- [18] A. Lacroix, G. T. De Laissardiere, P. Quémerais, J.-P. Julien, and D. Mayou, Modeling of Electronic Mobilities in Halide Perovskites: Adiabatic Quantum Localization Scenario, *Phys. Rev. Lett.* **124**, 196601 (2020).
- [19] T. A. Tyson, W. Gao, Y.-S. Chen, S. Ghose, and Y. Yan, Large thermal motion in halide perovskites, *Sci. Rep.* **7**, 1 (2017).
- [20] M. A. Carignano, S. A. Aravindh, I. S. Roqan, J. Even, and C. Katan, Critical fluctuations and anharmonicity in lead iodide perovskites from molecular dynamics supercell simulations, *J. Phys. Chem. C* **121**, 20729 (2017).
- [21] Y. Rakita, O. Bar-Elli, E. Meirzadeh, H. Kaslasi, Y. Peleg, G. Hodes, I. Lubomirsky, D. Oron, D. Ehre, and D. Cahen, Tetragonal $\text{CH}_3\text{NH}_3\text{PbI}_3$ is ferroelectric, *Proc. Natl. Acad. Sci. U.S.A.* **114**, E5504 (2017).
- [22] See Supplemental Material at <http://link.aps.org/supplemental/10.1103/PhysRevMaterials.4.092401> for supporting experimental and computational details.
- [23] M. Perrot, M. H. Brooker, and J. Lascombe, Raman light scattering studies of the depolarized Rayleigh wing of liquids and solutions, *J. Chem. Phys.* **74**, 2787 (1981).
- [24] O. F. Nielsen, The structure of liquid water. A low frequency ($10\text{--}400\text{ cm}^{-1}$) Raman study, *Chem. Phys. Lett.* **60**, 515 (1979).
- [25] K. Mizoguchi and S. I. Nakashima, Determination of crystallographic orientations in silicon films by Raman-microprobe polarization measurements, *J. Appl. Phys.* **65**, 2583 (1989).
- [26] W. Hayes and R. Loudon, *Scattering of Light by Crystals* (Dover, New York, 2004).
- [27] G. Burns and B. A. Scott, Raman Studies of Underdamped Soft Modes in PbTiO_3 , *Phys. Rev. Lett.* **25**, 167 (1970).
- [28] J. H. Parker, D. W. Feldman, and M. Ashkin, Raman scattering by silicon and germanium, *Phys. Rev.* **155**, 712 (1967).
- [29] G. A. Elbaz, W.-L. Ong, E. A. Doud, P. Kim, D. W. Paley, X. Roy, and J. A. Malen, Phonon speed, not scattering, differentiates thermal transport in lead halide perovskites, *Nano Lett.* **17**, 5734 (2017).
- [30] X. Qian, X. Gu, and R. Yang, Lattice thermal conductivity of organic-inorganic hybrid perovskite $\text{CH}_3\text{NH}_3\text{PbI}_3$, *Appl. Phys. Lett.* **108**, 063902 (2016).
- [31] A. D. Wright, C. Verdi, R. L. Milot, G. E. Eperon, M. A. Pérez-Osorio, H. J. Snaith, F. Giustino, M. B. Johnston, and L. M. Herz, Electron-phonon coupling in hybrid lead halide perovskites, *Nat. Commun.* **7**, 11755 (2016).
- [32] A. Putrino and M. Parrinello, Anharmonic Raman Spectra in High-Pressure Ice from *Ab Initio* Simulations, *Phys. Rev. Lett.* **88**, 176401 (2002).
- [33] T. Uchino and T. Yoko, Low-frequency Raman scattering and the fast relaxation process in glycerol, *Science* **273**, 480 (1996).
- [34] E. D. Gor'kovaya, Yu. A. Tikhonov, V. I. Torgashev, A. S. Mikheykin, I. A. Lukyanchuk, D. Mezzane, N. Ortega, A. Kumar, R. S. Katiyar, and A. G. Razumnyaya, Properties of the low-frequency phonon spectra of ferroelectric barium titanate-based heterostructures, *Ferroelectrics* **543**, 36 (2019).
- [35] K. P. Ong, T. W. Goh, Q. Xu, and A. Huan, Mechanical origin of the structural phase transition in methylammonium lead iodide $\text{CH}_3\text{NH}_3\text{PbI}_3$, *J. Phys. Chem. Lett.* **6**, 681 (2015).
- [36] J.-H. Lee, N. C. Bristowe, P. D. Bristowe, and A. K. Cheetham, Role of hydrogen-bonding and its interplay with octahedral tilting in $\text{CH}_3\text{NH}_3\text{PbI}_3$, *Chem. Commun.* **51**, 6434 (2015).
- [37] P. R. Varadwaj, A. Varadwaj, H. M. Marques, and K. Yamashita, Significance of hydrogen bonding and other noncovalent interactions in determining octahedral tilting in the $\text{CH}_3\text{NH}_3\text{PbI}_3$ hybrid organic-inorganic halide perovskite solar cell semiconductor, *Sci. Rep.* **9**, 50 (2019).
- [38] R. C. Remsing and M. L. Klein, Lone Pair Rotational Dynamics in Solids, *Phys. Rev. Lett.* **124**, 066001 (2020).
- [39] R. C. Remsing and M. L. Klein, A new perspective on lone pair dynamics in halide perovskites, *APL Mater.* **8**, 050902 (2020).
- [40] S. Y. Yue, X. Zhang, G. Qin, J. Yang, and M. Hu, Insight into the collective vibrational modes driving ultralow thermal conductivity of perovskite solar cells, *Phys. Rev. B* **94**, 115427 (2016).
- [41] H. Ma, Y. Ma, H. Wang, C. Slebodnick, A. Alatas, J. J. Urban, and Z. Tian, Experimental phonon dispersion and lifetimes of tetragonal $\text{CH}_3\text{NH}_3\text{PbI}_3$ perovskite crystals, *J. Phys. Chem. Lett.* **10**, 1 (2019).